

Impulsive source of the 2017, $M_W=7.3$, Ezgeleh, Iran, earthquake

B. Gombert^{1,2}, Z. Duputel², E. Shabani³, L. Rivera², R. Jolivet⁴, J. Hollingsworth⁵

¹Department of Earth Sciences, University of Oxford, U.K.

²Institut de Physique du Globe de Strasbourg, UMR7516, Université de Strasbourg, EOST/CNRS, France

³Department of Seismology, Institute of Geophysics, University of Tehran, Tehran, Iran

⁴Laboratoire de géologie, Département de Géosciences, École Normale Supérieure, PSL Research University, CNRS UMR 8538, Paris, France

⁵ISTerre/CNRS, UMR5275, Université Grenoble Alpes, Grenoble, France

Key Points:

- The Ezgeleh earthquake ruptured a flat thrust fault in the Zagros fold and thrust belt
- Kinematic slip modelling reveals a highly impulsive source with southward directivity, possibly causing the large damage in the area
- The direction of co-seismic slip suggests a strain partitioning between thrust and unmapped strike-slip faults

Corresponding author: Baptiste Gombert, baptiste.gombert@earth.ox.ac.uk

19 **Abstract**

20 On November 12th 2017, a $M_W=7.3$ earthquake struck near the Iranian town of
21 Ezgeleh, at the Iran-Iraq border. This event was located within the Zagros fold and thrust
22 belt which delimits the continental collision between the Arabian and Eurasian Plates.
23 Despite a high seismic risk, the seismogenic behaviour of the complex network of active
24 faults is not well documented in this area due to the long recurrence interval of large earth-
25 quakes. In this study, we jointly invert InSAR and near-field strong-motions to infer a
26 kinematic slip model of the rupture. The incorporation of these near-field observations
27 enables a fine resolution of the kinematic rupture process. It reveals an impulsive seis-
28 mic source with a strong southward rupture directivity, consistent with significant dam-
29 age south of the epicenter. We also show that the slip direction does not match plate con-
30 vergence, implying that some of the accumulated strain must be partitioned onto other
31 faults.

32 **Plain Language Summary**

33 Iran is a very seismically active region. However, the 2017 Ezgeleh earthquake of
34 magnitude 7.3 occurred in a region where large earthquakes have not been documented
35 for several centuries. Our knowledge of fault locations, geometries, and seismic behaviours
36 is therefore limited in this region. We use near-field seismological and satellite geode-
37 tic data to retrieve the spatial and temporal distribution of slip occurring on the fault
38 during the Ezgeleh earthquake. We show that the high slip rate and Southward direc-
39 tivity of the rupture may have worsen damage South of the epicentre. We also observe
40 that tectonic motion is partitioned between different type of faults. Although the Ezgeleh
41 earthquake did release a significant part of that strain, other seismogenic faults in the
42 region could represent an important hazard for nearby population.

43 **1 Introduction**

44 On November 12th, 2017, the Iranian province of Kermanshah and the Iraqi Kur-
45 distan were shaken by a severe $M_W=7.3$ earthquake located south of the border. It caused
46 the death of ~ 630 people and considerable damage, in particular in the Iranian city of
47 Sarpol-e Zahab (c.f. Figure 1). The earthquake triggered numerous landslides and rock
48 falls, including a massive 4x1 km landslide in Kermanshah (Miyajima et al., 2018).

49 The hypocenter is located within the Zagros Mountains near the Iranian town of
50 Ezgeleh, a tectonically active region that accommodates crustal shortening (e.g., Berberian & King, 1981) resulting from the collision between the Arabian Plate and the Eurasian
51 Plate. About a third to a half of current convergence is accommodated within the Za-
52 gros belt (Vernant et al., 2004). The belt hosts many moderate earthquakes ($M=5-6$)
53 with depths ranging from 4 km to 20 km, although this range is debated (e.g., Niazi et
54 al., 1978; Talebian & Jackson, 2004; Nissen et al., 2011). Our knowledge of the regional
55 seismo-tectonics is further complicated by the very rare occurrence of co-seismic surface
56 rupture (Talebian & Jackson, 2004; Walker et al., 2005).
57

58 The Ezgeleh earthquake occurred at the transition between the Lorestan Arc in the
59 south-east and the Kirkuk Embayment in the north-west (c.f. Figure 1). The area is cov-
60 ered by a 8-13 km thick sedimentary cover heavily folded into numerous anticlines (e.g.,
61 Falcon, 1969; Alavi, 2007). Sediments are crossed by many thrust faults that flatten within
62 the basement (Sadeghi & Yassaghi, 2016; Tavani et al., 2018). As expected from the lack
63 of surface ruptures and fault scarps, most of these faults are blind, hence the difficulty
64 to infer their geometry. In this region, plate convergence is roughly north-south (c.f., Fig-
65 ure 1) with a rate between 19 mm/yr (Kreemer et al., 2014) and 24 mm/yr (DeMets et
66 al., 2010). Slip is partitioned between thrust faults at the front of the belt, such as the
67 Mountain Front Fault, the High Zagros Fault and the Zagros Foredeep Fault, and the
68 Main Recent Fault, a right-lateral strike-slip fault located at the back of the belt (c.f.,
69 Figure 1; Berberian, 1995). This part of the Zagros belt hosts moderate seismicity, but
70 the last significant earthquakes ($5.9 \lesssim M \lesssim 6.4$) to strike the area happened in 958 and
71 1150 (Ambraseys & Melville, 2005). Therefore, our understanding of the regional seismo-
72 tectonic setting is obscured by the undersampled seismic cycle and the absence of ground
73 geodesy. The 2017 Ezgeleh earthquake highlighted the seismic hazard in this portion of
74 the Zagros belt. Its analysis hence provides a unique opportunity to enrich our under-
75 standing of the region and the associated seismic hazard. In addition, the availability
76 of near-field strong-motion records offers the possibility to closely study the propagation
77 of the rupture on the fault.

78 In this study, we propose a stochastic analysis of the 2017 earthquake source pro-
79 cess. We use a Bayesian framework to infer a population of co-seismic slip models that
80 fit available observations. While currently available studies were either limited to the static
81 final distribution of slip on the fault (He et al., 2018; Wanpeng et al., 2018; Barnhart et

82 al., 2018; Yang et al., 2018; Vajedian et al., 2018) or used far-field teleseismic data (Chen
83 et al., 2018; Nissen et al., 2019), we jointly invert InSAR and near-field strong-motion
84 data which provide a better resolution (Anderson, 2003) to propose a kinematic descrip-
85 tion of the earthquake source. We use a layered velocity model that is routinely used to
86 locate earthquakes by the IRSC (Iranian Seismological Center), which ensures modelling
87 is performed to the best of our knowledge (Supplementary Table T1).

88 **2 Inversion of co-seismic slip**

89 **2.1 Observations**

90 Due to the remote location of the event, the only available geodetic data come from
91 interferometric Synthetic Aperture Radar (InSAR). We use three SAR interferograms
92 computed from acquisition by the Sentinel-1 satellite, along two ascending and one de-
93 scending tracks (Figures 2a and S1-2). We use the ISCE software with precise orbits and
94 SRTM DEM to compute the co-seismic interferograms (Rosen et al., 2012). The coher-
95 ence of the radar phase is excellent, likely due to the arid conditions of this region. Ac-
96 quisition dates are available in Table T2. We measure up to 80 cm of ground displace-
97 ment toward the satellite in the ascending tracks, suggesting uplift and/or displacement
98 toward the south-west. The number of data points in the unwrapped interferograms is
99 reduced using a recursive quad-tree algorithm (cf., Figure S1; Lohman & Simons, 2005).
100 We estimate uncertainties due to tropospheric perturbations in the phase by estimat-
101 ing empirical covariance functions for each interferograms (Jolivet et al., 2014). Estimated
102 covariance parameters are summarized in Table T2.

103 We include near-field seismic waveforms recorded by 10 strong-motion accelerom-
104 eters from the Iran Strong Motion Network (ISMN) to constrain the temporal evolution
105 of slip during the earthquake rupture. Although located only on one side of the rupture,
106 all stations are within 102 km of the epicentre (c.f. Figure 2b). Details on strong mo-
107 tion data processing are given in Supplementary Text T1 (Ide, 2007; Lee & Lahr, 1972).
108 The east component of the two stations located south of the rupture (SPZ and GRS)
109 was not used due to the poor quality of the record. We integrate accelerometric data to
110 recover ground velocity, downsampled to 1 sps. Waveforms are bandpass filtered between
111 7 s and 50 s using a 4th order Butterworth band-pass filter, then windowed around the
112 first arrivals.

113 **2.2 Estimation of the fault plane**

114 The two nodal planes of the global CMT mechanism (Ekström et al., 2005) are ei-
115 ther a shallow north-east dipping plane (351° strike and 11° dip) or a nearly vertical
116 plane (121° strike and 83° dip). We conduct a grid-search on fault geometry param-
117 eters for each nodal plane. The goal is to discriminate between the two planes and to
118 find the optimal fault geometry to limit forward modelling errors.

119 We grid-search the fault location and its strike and dip angles by inverting the In-
120 SAR displacement to find the geometry that better explains the observations. For each
121 tested geometry, slip is inverted on 96 subfault patches using a simple least-square tech-
122 nique. More details on the method are given in Supplementary text T2 (Tarantola, 2005).
123 We find that even the best sub-vertical plane has a RMS six times larger than the shallow-
124 dipping plane (c.f. Figures S4 and S5). Although the sub-vertical plane is compatible
125 with a back-thrust fault that may exist in the region (Tavani et al., 2018) or with the
126 reactivation of steep normal faults (Jackson, 1980), the shallow dipping plane is in bet-
127 ter agreement with receiver functions analysis (Paul et al., 2010) and the tectonic set-
128 ting (e.g. Berberian, 1995; Vergés et al., 2011). Our optimal plane (351° strike, 14° dip,
129 13 km depth) agrees well with other studies using a similar grid-search approach (Barn-
130 hart et al., 2018; Wanpeng et al., 2018). In the following, we will consider that the Ezgeleh
131 earthquake occurred on our optimum shallow dipping plane.

132 **2.3 Co-seismic slip modelling**

133 We use fault parameters inferred in section 2.2 to construct a planar fault and di-
134 vide it in 96 subfault patches, each with a dimension of 7x7 km². Patch size was deter-
135 mined through trial and error to limit correlation between slip on neighbouring parts of
136 the fault. Source model parameters include total final slip, rupture velocity, and rise time
137 for each patch along with hypocenter location. We define \mathbf{m}_S the vector including the
138 two components of static slip (i.e. final integrated slip), and \mathbf{m}_K the vector of kinematic
139 parameters describing the temporal evolution of slip.

140 We solve the problem in a Bayesian framework using AlTar, a Markov Chain Monte
141 Carlo algorithm based on the algorithm described by Minson et al. (2013). It samples
142 the full posterior probability distribution of the models that fit observations and are con-
143 sistent with prior information. The strength of our solution is that it does not rely on

144 any spatial smoothing and provides accurate estimates of the posterior slip uncertainty.
 145 We sample the posterior probability density $p(\mathbf{m}_S, \mathbf{m}_K | \mathbf{d}_S, \mathbf{d}_K)$ given by

$$146 \quad p(\mathbf{m}_S, \mathbf{m}_K | \mathbf{d}_S, \mathbf{d}_K) \propto p(\mathbf{m}_K) p(\mathbf{m}_S) p(\mathbf{d}_S | \mathbf{m}_S) p(\mathbf{d}_K | \mathbf{m}_S, \mathbf{m}_K) \quad (1)$$

147 where \mathbf{d}_S and \mathbf{d}_K are the InSAR and strong-motion observations, respectively. The prior
 148 PDFs $p(\mathbf{m}_S)$ and $p(\mathbf{m}_K)$ are mostly uniform distributions designed to prevent some model
 149 features such as back-slip. They are described in details in Table T3. For further details
 150 on the method, the reader can refer to Supplementary text T3, Herrmann (2013); Du-
 151 putel et al. (2014); Minson et al. (2013) and Gombert et al. (2018).

152 **3 Results**

153 In the first seconds following the hypocentral time, slip propagates in every direc-
 154 tion around the hypocentre (c.f. Figure 3 and supplementary movie M1). Approximately
 155 5 seconds after origin, the rupture almost only propagates toward the south. The largest
 156 slip rate occurs roughly after 6 seconds, 20 km south of the epicentre. We observe a strong
 157 directivity toward the south, consistent with a shorter, higher amplitude signal at sta-
 158 tions SPZ and GRS compared to stations located in the north (c.f., Figures 2 and S3).
 159 In addition, we infer a large slip rate on the fault. As shown in Figures 4d-e and S6, slip
 160 rate increases up to more than 3 m/s where the slip is maximum. The slip rate functions
 161 of two fault patches presented here show the fast increase in slip rate associated with a
 162 short rise time ≤ 5 s, defining a sharp slip pulse (Heaton, 1990). Although larger than
 163 the values usually reported in kinematic slip models (usually ranging from 0.1 m/s to
 164 1 m/s), our slip rate estimates for this event are compatible with well documented earth-
 165 quakes (e.g., Minson et al., 2014; Cirella et al., 2012). The fast slip rate of the fault is
 166 reflected in the moment rate function (MRF) shown in Figure 3c. To obtain the MRF,
 167 we first calculate the scalar moment function, $M_0(t)$, by summing the moment tensor
 168 function of each subfault and using definition of the scalar moment from Dahlen & Tromp
 169 (1998). The MRF is then obtained using the time-derivative of $M_0(t)$. As shown in Fig-
 170 ure 3c, 90% of the moment was released within the first 14 seconds of the rupture, de-
 171 picting an overall impulsive earthquake. The mean rupture speed along-strike is $3.0 \pm$
 172 0.25 km/s (Figure S7), which is $\sim 0.9V_s$ at that depth.

173 The posterior mean model of the final cumulative slip is shown in Figure 4a. At
 174 first order, this solution is in agreement with previously published static models (Barn-

175 hart et al., 2018; Wanpeng et al., 2018). We infer a ~ 50 km long and ~ 30 km wide rup-
176 ture, with a peak slip of $5.5 \text{ m} \pm 0.5 \text{ m}$. One difference arises as previous models proposed
177 that two distinct asperities ruptured during the earthquake. Our posterior mean model
178 does not show a clearly distinct rupture area in the north, closer to the hypocenter. How-
179 ever, roughly 20% of the models in our solution present such a feature (see Supplemen-
180 tary Movie M2). This indicates that it is in the realm of possibilities but available ob-
181 servations cannot entirely resolve it. The slip direction is constant along most of the fault,
182 with a $131.5^\circ \pm 0.8^\circ$ rake corresponding to a motion toward the south-west. The inferred
183 focal mechanism is therefore consistent with long-period moment tensor inversions.

184 Our Bayesian framework allows us to directly infer the posterior uncertainties as-
185 sociated with the model parameters. Slip uncertainties are represented in Figure 4a by
186 the 95% confidence ellipses. In addition, posterior marginal distributions after the static
187 and kinematic inversions of the along-rake slip of two fault patches are shown in 4b-c.
188 Unsurprisingly, the inclusion of kinematic observations reduces the posterior uncertain-
189 ties of those parameters. On the highest slipping patch for instance, the $1-\sigma$ posterior
190 uncertainty decreases from 0.82 m to 0.52 m. Over the fault, we observe a rather low pos-
191 terior uncertainty at shallow and intermediate depths, where slip is located. At depths
192 larger than 15 km, uncertainties become more significant. However, the inspection of each
193 model composing the solution reveals a good consistency in the slip distribution, with
194 nonetheless a larger variability in the northern part of the rupture (c.f., supplementary
195 movie M2). This is confirmed by our analysis of the model ensemble revealing that data
196 provides more information where the fault experienced large slip (cf., Supplementary text
197 T4 and Figure S8).

198 As shown in Figures S1, S2 and S9, model predictions fit Sentinel-1A observations
199 very well. Residuals are small over the three tracks, and they are consistent with the am-
200 plitude of 5-7 days of post-seismic signal (~ 10 cm; Barnhart et al., 2018). Stochastic model
201 predictions of the strong-motion data are shown in Figures 2 and S3. Overall, our so-
202 lution can explain the observations with a good accuracy. Posterior model predictions
203 of stations KAT, SNI and MHD suffer from larger uncertainties, likely explained by their
204 greater distance from the hypocenter.

4 Discussion

As suggested by previous studies (Barnhart et al., 2018; He et al., 2018; Wanpeng et al., 2018), the Ezgeleh earthquake likely occurred on the Mountain Flexure Fault (sometimes referred as Main Front Fault, noted MFF in Figure 1). Along the major part of the Zagros belt, the MFF follows a NW-SE axis with a $\sim 120^\circ$ azimuth and is aligned with many topographic features (visible on the DEM in Figure 4). However, the strike of the fault differs by about 50° with the topography orientation at the location of the earthquake. This discrepancy is explained by a major bend in the MFF at this location as it transitions between the Lurestan Arc (LA) in the south and the Kirkuk Embayment (KE) in the north (e.g., Koshnaw et al., 2017; Vergés et al., 2011). Interestingly, the fault bend between the LA and KE corresponds to the northern bound of the rupture (Figure 3). This geometry change possibly stopped the rupture propagation, as suggested by numerical models (Aochi et al., 2000). The rupture may also have been halted by the 8 km to 10 km thick sediment cover, whose depth roughly corresponds to the updip limit of slip. Although poorly constrained, these boundaries could nonetheless help to better assess the probable size for future large events in the region, a valuable element in seismic hazard assessment (e.g., Hetényi et al., 2016).

These sediments are heavily folded in the forearc basin and host many large anticlines (e.g., Kent, 2010; Casciello et al., 2009). These folds are evidence for thin-skin shortening occurring within the belt (Koshnaw et al., 2017). However, the slip of the 2017 earthquake occurred at larger depth, between 10 km and 15 km. This deeper co-seismic deformation suggests that thick-skin shortening is also happening in this part of the Zagros range (Nissen et al., 2011; Vergés et al., 2011). The slip direction of the Ezgeleh earthquake on the MFF is nearly perpendicular to the alignment of the topographic features mentioned above (cf., Figure 4a), creating a maximum 65 cm of uplift and 33 cm of subsidence across the belt (c.f., Figure S10). Despite the relatively large depth of the Ezgeleh earthquake, such co-seismic deformation may thus contribute to the growth of the Zagros topography. Afterslip might also contribute although it seems to occur on a shallow dipping decollement at the front of the mountain range (Barnhart et al., 2018).

An interesting feature of the Ezgeleh earthquake is the discrepancy between the co-seismic slip direction and the current plate motion. Both the GSRM v2.1 model (Kreemer et al., 2014) and the MORVEL model (DeMets et al., 2010) predict a nearly N-S plate

237 convergence (see Figure 1) while the overall co-seismic slip vector is oriented on a S 30° W
238 axis (see Figure 4).

239 This difference suggests that strain partitioning is occurring in this part of the Za-
240 gros belt, with a partial decoupling between the thrust and right-lateral strike-slip mo-
241 tion (Platt, 1993; McCaffrey, 1992). Strain partitioning in the Lurestan Arc and the Kirkuk
242 Embayment has been proposed before based on the analysis of regional focal mechanisms
243 (Talebian & Jackson, 2004). The Main Recent Fault (MRF; see Figure 1) is a major NW-
244 SE, 800 km long right-lateral strike-slip fault which accommodates some of the strain
245 (Tchalenko & Braud, 1974). It hosted several large earthquakes and has a ~50 km hor-
246 izontal offset (Talebian & Jackson, 2002). However, other structures may be accommo-
247 dating the strike-slip component of the convergence. Between July and November 2018,
248 three significant aftershocks with respective magnitudes of $M_W=5.8$, $M_W=6.0$, and $M_W=6.2$
249 occurred south of the mainshock epicenter (c.f. Figure 1b). These events present a right-
250 lateral strike-slip focal mechanism, but are located more than 100 km west of the MRF.
251 They could have ruptured the Khanaqin fault, a N-S strike-slip structure marking the
252 boundary between the Lurestan Arc and the Kirkuk Embayment (e.g., Blanc et al., 2003;
253 Hessami et al., 2001; Berberian, 1995). However, there is very limited evidence that the
254 Khanaqin fault is actually a strike-slip fault. As a matter of fact, a recent study by Ta-
255 vani et al. (2018) using reconstruction of seismic profiles proposed that the Khanaqin
256 fault is a back-thrust structure accommodating the SW-NE motion. Therefore, unde-
257 tected strike-slip faults may be accommodating some of the strike-slip deformation closer
258 to the forearc than the MRF. Throughout the Zagros, the MRF is known to accommo-
259 date a major component of the northward motion via strain partitioning (Talebian &
260 Jackson, 2002). However, not all the regional shear is accommodated solely on the MRF,
261 especially along its northwest limit, where strike-slip faulting becomes increasingly dis-
262 tributed (Copley & Jackson, 2006). The additional contribution from other less-known
263 active structures in this region therefore poses an important uncharacterized seismic risk
264 for local populations.

265 While the rupture directivity imaged here is visible in published slip models (Chen
266 et al., 2018; Nissen et al., 2019), the sharpness of the slip pulse in these studies is blurred
267 by their use of far-field data and smoothing constraints. The good spatial and tempo-
268 ral resolution of our kinematic slip model enabled by the use of near-field observations
269 reveals interesting features. Figures 3 and S6 show that the rupture starts as a growing

270 crack that rapidly transition into a pulse with a rise time of about 4 sec. This crack-pulse
271 transition occurs within the first four seconds and less than 7 km from the hypocenter,
272 therefore away from the rupture boundaries. Day (1982) proposed that if the slip rate
273 is controlled by the fault geometry the rise time should be $T_R = 0.5 \times W/V_R$, with W
274 the fault width and V_R the rupture velocity. However, we infer T_R values systematically
275 higher than inverted rise times (Figure S11). This pulse-like behaviour is therefore un-
276 likely to result from healing phases emanating from the along-dip finiteness of the fault.
277 A rapid crack-pulse transition is in agreement with early observations by Heaton (1990)
278 and later studies (e.g., Wang et al., 2019; Beroza & Mikumo, 1996; Meier et al., 2016).
279 Such a pulse may result from a number of mechanisms such as frictional self-healing, fault
280 strength or stress heterogeneities, bimaterial effects and wave reflections within low-velocity
281 fault zones (e.g., Perrin et al., 1995; Andrews & Ben-Zion, 1997; Huang & Ampuero, 2011).
282 After this early transition from a growing crack, the rupture continues its journey along-
283 strike as a decaying pulse toward the north, and a strong growing pulse toward the south.

284 This strong southward propagating pulse seems to have a significant impact in the
285 distribution of damage and landslides triggered by the earthquake. The Ezgeleh earth-
286 quake induced extensive destructions of dwellings in Iraqi Kurdistan, but mostly in the
287 Iranian province of Kermanshah. Figure 1b) shows the intensity of damage created by
288 the mainshock. It is obtained from field observations conducted by the International In-
289 stitute of Earthquake Engineering and Seismology of Iran (IIEES). Reported macroseis-
290 mic intensities are also shown in Figure S12. Damage intensity roughly follows the sur-
291 face projection of the slip distribution, but larger damage was reported in the south. In
292 addition to building damage, many rockfalls and landslides occurred south of the rup-
293 ture and up to 125 km from the centroid, including a large 4 km long and 1 km wide land-
294 slide (Miyajima et al., 2018). These observations may however be biased by the difficulty
295 to report such phenomena on the Iraqi side of the border. Many different factors can also
296 largely influence the effects of an earthquake, like soil nature or mountain slopes. In ad-
297 dition to rupture directivity, studies have suggested that the strong impulsiveness of the
298 source can intensify low-frequency ground shaking, particularly damaging to buildings
299 (Melgar & Hayes, 2017; Somerville & Graves, 2003). The large slip-rate and short rise-
300 time of the southward propagating pulse may therefore have exacerbated the damage
301 observed south-west of the Ezgeleh earthquake.

302 **5 Conclusion**

303 The 2017 Ezgeleh earthquake breaks a long hiatus on strong events affecting the
304 Zagros thrust and fold belt in the Kermanshah province. The joint inversion of InSAR
305 and near-field strong-motion observations reveals a predominantly thrust motion on a
306 near-horizontal blind crustal fault. We also infer a highly impulsive source propagating
307 toward the south. These kinematic properties may have played a role in the numerous
308 slope instabilities and in the important damage that affected Iranian cities.

309 Furthermore, the misalignment between the plate convergence and the slip direc-
310 tion provide additional hints for a strain partitioning in this part of the Zagros belt be-
311 tween thrust motion on flat crustal faults and right-lateral strike-slip. As suggested by
312 late aftershocks, unmapped dextral faults could be accommodating part of that shear
313 strain, and therefore represent an important seismic risk for nearby populations.

314 **Acknowledgments**

315 This project has received funding from the European Research Council (ERC) under the
316 European Union's Horizon 2020 research and innovation programme under grant agree-
317 ments No 758210 and No 805256. This work also received financial support of Agence
318 Nationale de la Recherche (project ANR-17-ERC3-0010). The Copernicus Sentinel-1 data
319 were provided by the European Space Agency (ESA). Seismological observations belong
320 to the Iran Strong Motion Network (<https://ismn.bhrc.ac.ir/en>). We acknowledge
321 the Geological Survey of Iran (Seismotectonics and Seismology group) for making avail-
322 able their preliminary report (in persian). It can be obtained upon request to info@gsi.ir.
323 The AlTar algorithm used for the inversion was developed by the Seismological Labo-
324 ratory at Caltech and was provided by Mark Simons. We thank the editor, Gavin Hayes,
325 and two anonymous reviewers for their constructive comments which helped improve this
326 manuscript.

References

- 327
328 Alavi, M. (2007). Structures of the Zagros fold-thrust belt in Iran. *American Jour-*
329 *nal of science*, *307*(9), 1064–1095.
- 330 Ambraseys, N. N., & Melville, C. P. (2005). *A history of Persian earthquakes*. Cam-
331 bridge university press.
- 332 Anderson, J. G. (2003). Strong-motion seismology. *INTERNATIONAL GEO-*
333 *PHYSICS SERIES*, *81*(B), 937–966.
- 334 Andrews, D. J., & Ben-Zion, Y. (1997). Wrinkle-like slip pulse on a fault between
335 different materials. *Journal of Geophysical Research: Solid Earth*, *102*(B1), 553–
336 571.
- 337 Aochi, H., Fukuyama, E., & Matsuura, M. (2000). Spontaneous rupture propagation
338 on a non-planar fault in 3-D elastic medium. *pure and applied geophysics*, *157*(11-
339 12), 2003–2027.
- 340 Barnhart, W. D., Brengman, C. M., Li, S., & Peterson, K. E. (2018). Ramp-
341 flat basement structures of the Zagros Mountains inferred from co-seismic
342 slip and afterslip of the 2017 Mw7.3 Darbandikhan, Iran/Iraq earthquake.
343 *Earth and Planetary Science Letters*, *496*, 96 - 107. Retrieved from [http://](http://www.sciencedirect.com/science/article/pii/S0012821X18303194)
344 www.sciencedirect.com/science/article/pii/S0012821X18303194 doi:
345 <https://doi.org/10.1016/j.epsl.2018.05.036>
- 346 Berberian, M. (1995). Master blind thrust faults hidden under the Zagros folds:
347 active basement tectonics and surface morphotectonics. *Tectonophysics*, *241*(3-4),
348 193–224.
- 349 Berberian, M., & King, G. C. P. (1981). Towards a paleogeography and tectonic evo-
350 lution of Iran. *Canadian Journal of Earth Sciences*, *18*(2), 210265. doi: 10.1139/
351 e81-019
- 352 Beroza, G. C., & Mikumo, T. (1996). Short slip duration in dynamic rupture in the
353 presence of heterogeneous fault properties. *Journal of Geophysical Research: Solid*
354 *Earth*, *101*(B10), 22449–22460.
- 355 Blanc, E.-P., Allen, M. B., Inger, S., & Hassani, H. (2003). Structural styles in the
356 Zagros simple folded zone, Iran. *Journal of the Geological Society*, *160*(3), 401–
357 412.
- 358 Casciello, E., Vergés, J., Saura, E., Casini, G., Fernández, N., Blanc, E., ... Hunt,
359 D. (2009). Fold patterns and multilayer rheology of the Lurestan Province, Zagros

- 360 simply folded belt (Iran). *Journal of the Geological Society*, 166(5), 947–959.
- 361 Chen, K., Xu, W., Mai, P. M., Gao, H., Zhang, L., & Ding, X. (2018). The 2017
362 Mw 7.3 Sarpol Zahāb Earthquake, Iran: A compact blind shallow-dipping thrust
363 event in the mountain front fault basement. *Tectonophysics*.
- 364 Cirella, A., Piatanesi, A., Tinti, E., Chini, M., & Cocco, M. (2012). Complexity of
365 the rupture process during the 2009 L’Aquila, Italy, earthquake. *Geophysical Jour-
366 nal International*, 190(1), 607–621.
- 367 Copley, A., & Jackson, J. (2006). Active tectonics of the Turkish-Iranian plateau.
368 *Tectonics*, 25(6).
- 369 Dahlen, F., & Tromp, J. (1998). *Theoretical global seismology*. Princeton university
370 press.
- 371 Day, S. M. (1982). Three-dimensional finite difference simulation of fault dynamics:
372 rectangular faults with fixed rupture velocity. *Bulletin of the Seismological Society
373 of America*, 72(3), 705–727.
- 374 DeMets, C., Gordon, R. G., & Argus, D. F. (2010). Geologically current plate mo-
375 tions. *Geophysical Journal International*, 181(1), 1–80.
- 376 Duputel, Z., Agram, P. S., Simons, M., Minson, S. E., & Beck, J. L. (2014, April).
377 Accounting for prediction uncertainty when inferring subsurface fault slip. *Geo-
378 phys. J. Int.*, 197(1), 464–482.
- 379 Ekström, G., Dziewonski, A. M., Maternovskaya, N. N., & Nettles, M. (2005, Febru-
380 ary). Global seismicity of 2003: centroid–moment–tensor solutions for 1087 earth-
381 quakes. *Phys. Earth Planet. Inter.*, 148(2-4), 327–351.
- 382 Ekström, G., Nettles, M., & Dziewonski, A. M. (2012, June). The global CMT
383 project 2004–2010: Centroid-moment tensors for 13,017 earthquakes. , 200-201,
384 1–9.
- 385 Falcon, N. L. (1969). Problems of the relationship between surface structure and
386 deep displacements illustrated by the Zagros Range. *Geological Society, London,
387 Special Publications*, 3(1), 9–21.
- 388 Farr, T. G., Rosen, P. A., Caro, E., Crippen, R., Duren, R., Hensley, S., ... others
389 (2007). The shuttle radar topography mission. *Reviews of geophysics*, 45(2).
- 390 Gombert, B., Duputel, Z., Jolivet, R., Simons, M., Jiang, J., Liang, C., ... Rivera,
391 L. (2018). Strain budget of the Ecuador–Colombia subduction zone: A stochastic
392 view. *Earth and Planetary Science Letters*, 498, 288–299.

- 393 GSI. (2017). *Preliminary report on geological features of the Ezgaleh-Kermanshah*
394 *earthquake (M 7.3), November 12, 2017, West Iran. GSI preliminary report num-*
395 *ber: 17-01, ver.03* (Tech. Rep.).
- 396 He, P., Wen, Y., Xu, C., & Chen, Y. (2018). High-quality three-dimensional dis-
397 placement fields from new-generation SAR imagery: application to the 2017
398 Ezgaleh, Iran, earthquake. *Journal of Geodesy*, 1–19.
- 399 Heaton, T. H. (1990). Evidence for and implications of self-healing pulses of slip in
400 earthquake rupture. *Physics of the Earth and Planetary Interiors*, 64(1), 1–20.
- 401 Herrmann, R. B. (2013, November). Computer Programs in Seismology: An Evolv-
402 ing Tool for Instruction and Research. *Seismol. Res. Lett.*, 84(6), 1081–1088.
- 403 Hessami, K., Koyi, H., & Talbot, C. J. (2001). The significance of strike-slip faulting
404 in the basement of the Zagros fold and thrust belt. *Journal of petroleum Geology*,
405 24(1), 5–28.
- 406 Hetényi, G., Cattin, R., Berthet, T., Le Moigne, N., Chopel, J., Lechmann, S., ...
407 others (2016). Segmentation of the Himalayas as revealed by arc-parallel gravity
408 anomalies. *Scientific reports*, 6, 33866.
- 409 Huang, Y., & Ampuero, J.-P. (2011). Pulse-like ruptures induced by low-velocity
410 fault zones. *Journal of Geophysical Research: Solid Earth*, 116(B12).
- 411 Ide, S. (2007). Slip inversion. In *Treatise on geophysics* (Vol. 4, pp. 193–224). Else-
412 vier. doi: <https://doi.org/10.1016/B978-0-444-53802-4.00076-2>
- 413 ISMN. (2018). *Iranian Strong Motion Network, Housing, and Urban Development*
414 *Research Center*. <https://ismn.bhrc.ac.ir/en>. doi: 10.7914/SN/II
- 415 Jackson, J. (1980). Reactivation of basement faults and crustal shortening in oro-
416 genic belts. *Nature*, 283(5745), 343–346.
- 417 Jolivet, R., Duputel, Z., Riel, B., Simons, M., Rivera, L., Minson, S., ... others
418 (2014). The 2013 M w 7.7 Balochistan earthquake: Seismic potential of an
419 accretionary wedge. *Bulletin of the Seismological Society of America*, 104(2),
420 1020–1030.
- 421 Kent, W. N. (2010). Structures of the Kirkuk Embayment, northern Iraq: foreland
422 structures or Zagros Fold Belt structures. *GeoArabia*, 15(4), 147–188.
- 423 Koshnaw, R. I., Horton, B. K., Stockli, D. F., Barber, D. E., Tamar-Agha, M. Y.,
424 & Kendall, J. J. (2017). Neogene shortening and exhumation of the Zagros
425 fold-thrust belt and foreland basin in the Kurdistan region of northern Iraq.

- 426 *Tectonophysics*, 694, 332–355.
- 427 Kreemer, C., Blewitt, G., & Klein, E. C. (2014). A geodetic plate motion and Global
428 Strain Rate Model. *Geochemistry, Geophysics, Geosystems*, 15(10), 3849–3889.
- 429 Lee, W. H. K., & Lahr, J. C. (1972). *HYPO71: A computer program for determin-*
430 *ing hypocenter, magnitude, and first motion pattern of local earthquakes* (Tech.
431 Rep.). US Geological Survey,.
- 432 Lohman, R. B., & Simons, M. (2005, January). Some thoughts on the use of In-
433 SAR data to constrain models of surface deformation: Noise structure and data
434 downsampling. *Geochem. Geophys. Geosyst.*, 6(1), Q01007.
- 435 McCaffrey, R. (1992). Oblique plate convergence, slip vectors, and forearc deforma-
436 tion. *Journal of Geophysical Research: Solid Earth*, 97(B6), 8905–8915.
- 437 Meier, M.-A., Heaton, T., & Clinton, J. (2016). Evidence for universal earthquake
438 rupture initiation behavior. *Geophysical Research Letters*, 43(15), 7991–7996.
- 439 Melgar, D., & Hayes, G. P. (2017). Systematic observations of the slip pulse prop-
440 erties of large earthquake ruptures. *Geophysical Research Letters*, 44(19), 9691–
441 9698.
- 442 Minson, S., Simons, M., & Beck, J. (2013). Bayesian inversion for finite fault earth-
443 quake source models I Theory and algorithm. *Geophysical Journal International*,
444 194(3), 1701–1726.
- 445 Minson, S., Simons, M., Beck, J., Ortega, F., Jiang, J., Owen, S., ... Sladen, A.
446 (2014). Bayesian inversion for finite fault earthquake source models–II: the 2011
447 great Tohoku-oki, Japan earthquake. *Geophysical Journal International*, 198(2),
448 922–940.
- 449 Miyajima, M., Fallahi, A., Ikemoto, T., Samaei, M., Karimzadeh, S., Setiawan, H.,
450 ... Karashi, J. (2018). Site Investigation of the Sarpole-Zahab Earthquake, Mw
451 7.3 in SW Iran of November 12, 2017. *JSCE Journal of Disaster, FactSheet:*
452 *FS2018-E-0002*.
- 453 Niazi, M., Asudeh, I., Ballard, G., Jackson, J., King, G., & McKenzie, D. (1978).
454 The depth of seismicity in the Kermanshah region of the Zagros Mountains (Iran).
455 *Earth and Planetary Science Letters*, 40(2), 270–274.
- 456 Nissen, E., Ghods, A., Karasözen, E., Elliott, J. R., Barnhart, W. D., Bergman,
457 E. A., ... others (2019). The 12 November 2017 M w 7.3 Ezgeleh–Sarpolzahab
458 (Iran) earthquake and active tectonics of the Lurestan arc. *Journal of Geophysical*

459 *Research: Solid Earth.*

460 Nissen, E., Tatar, M., Jackson, J. A., & Allen, M. B. (2011). New views on earth-
461 quake faulting in the Zagros fold-and-thrust belt of Iran. *Geophysical Journal In-*
462 *ternational*, 186(3), 928–944.

463 Paul, A., Hatzfeld, D., Kaviani, A., Tatar, M., & Péquegnat, C. (2010). Seismic
464 imaging of the lithospheric structure of the Zagros mountain belt (Iran). *Geologi-*
465 *cal Society, London, Special Publications*, 330(1), 5–18.

466 Perrin, G., Rice, J. R., & Zheng, G. (1995). Self-healing slip pulse on a frictional
467 surface. *Journal of the Mechanics and Physics of Solids*, 43(9), 1461–1495.

468 Platt, J. (1993). Mechanics of oblique convergence. *Journal of Geophysical Research:*
469 *Solid Earth*, 98(B9), 16239–16256.

470 Rosen, P. A., Gurrola, E., Sacco, G. F., & Zebker, H. (2012). The InSAR scien-
471 tific computing environment. In *Synthetic aperture radar, 2012. eusar. 9th euro-*
472 *pean conference on* (pp. 730–733).

473 Sadeghi, S., & Yassaghi, A. (2016). Spatial evolution of Zagros collision zone in Kur-
474 distan, NW Iran: constraints on Arabia–Eurasia oblique convergence. *Solid Earth*,
475 7(2), 659–659.

476 Somerville, P., & Graves, R. (2003). Characterization of earthquake strong ground
477 motion. In *Landslide tsunamis: Recent findings and research directions* (pp. 1811–
478 1828). Springer.

479 Talebian, M., & Jackson, J. (2002). Offset on the Main Recent Fault of NW Iran
480 and implications for the late Cenozoic tectonics of the Arabia–Eurasia collision
481 zone. *Geophysical Journal International*, 150(2), 422–439.

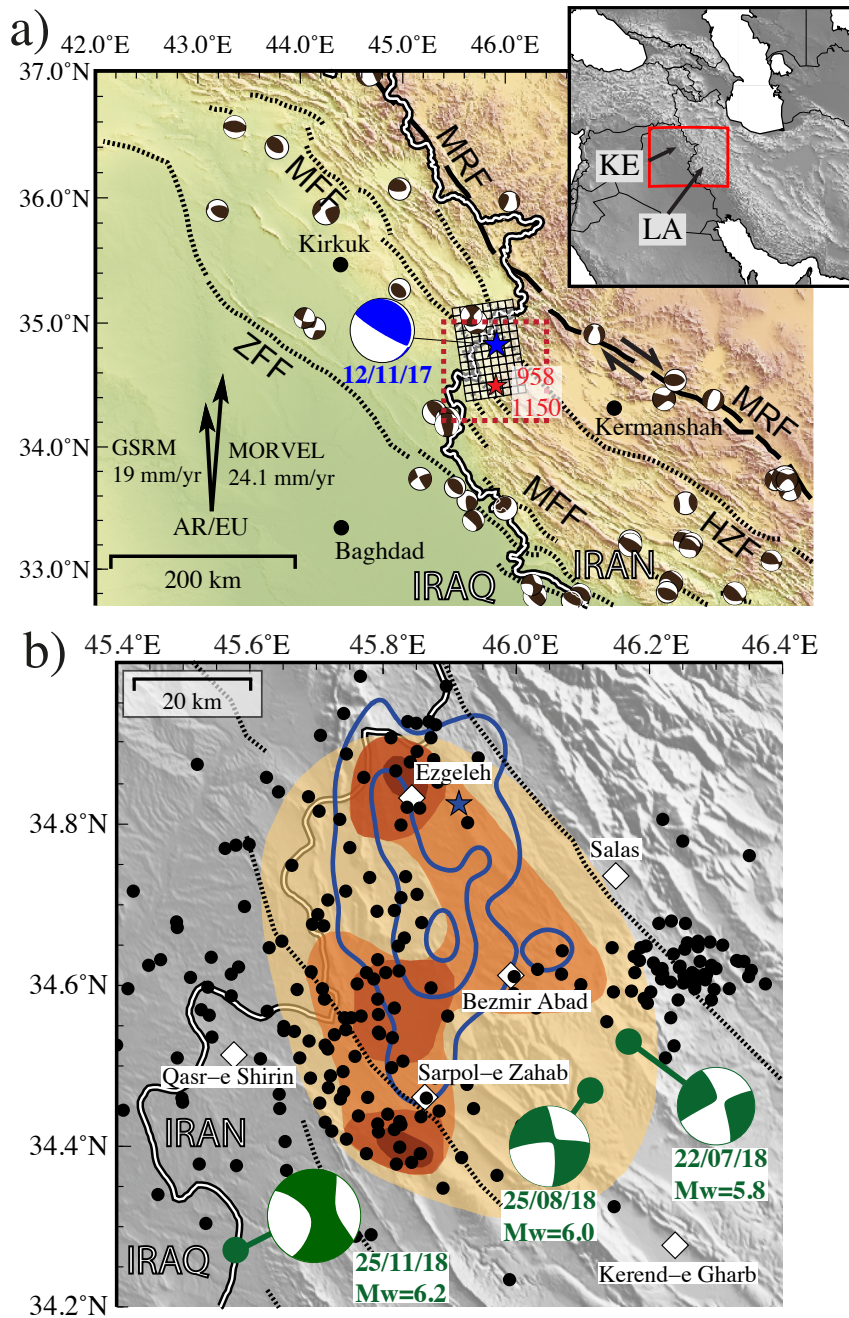
482 Talebian, M., & Jackson, J. (2004). A reappraisal of earthquake focal mechanisms
483 and active shortening in the Zagros mountains of Iran. *Geophysical Journal Inter-*
484 *national*, 156(3), 506–526.

485 Tarantola, A. (2005). *Inverse problem theory and methods for model parameter esti-*
486 *mation* (Vol. 89). siam.

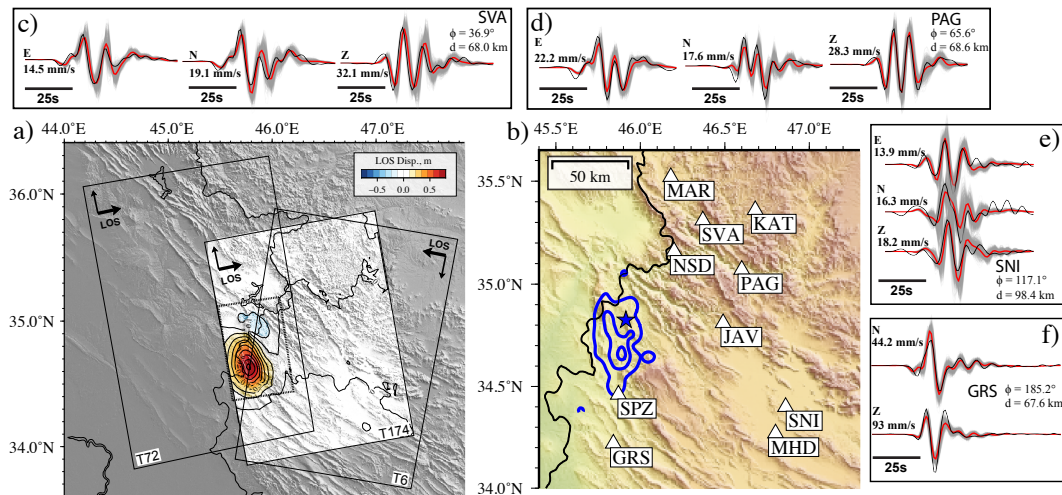
487 Tavani, S., Parente, M., Puzone, F., Corradetti, A., Gharabeigli, G., Valinejad,
488 M., . . . Mazzoli, S. (2018). The seismogenic fault system of the 2017 M w 7.3
489 Iran–Iraq earthquake: constraints from surface and subsurface data, cross-section
490 balancing, and restoration. *Solid Earth*, 9(3), 821.

491 Tchalenko, J., & Braud, J. (1974). Seismicity and structure of the Zagros (Iran):

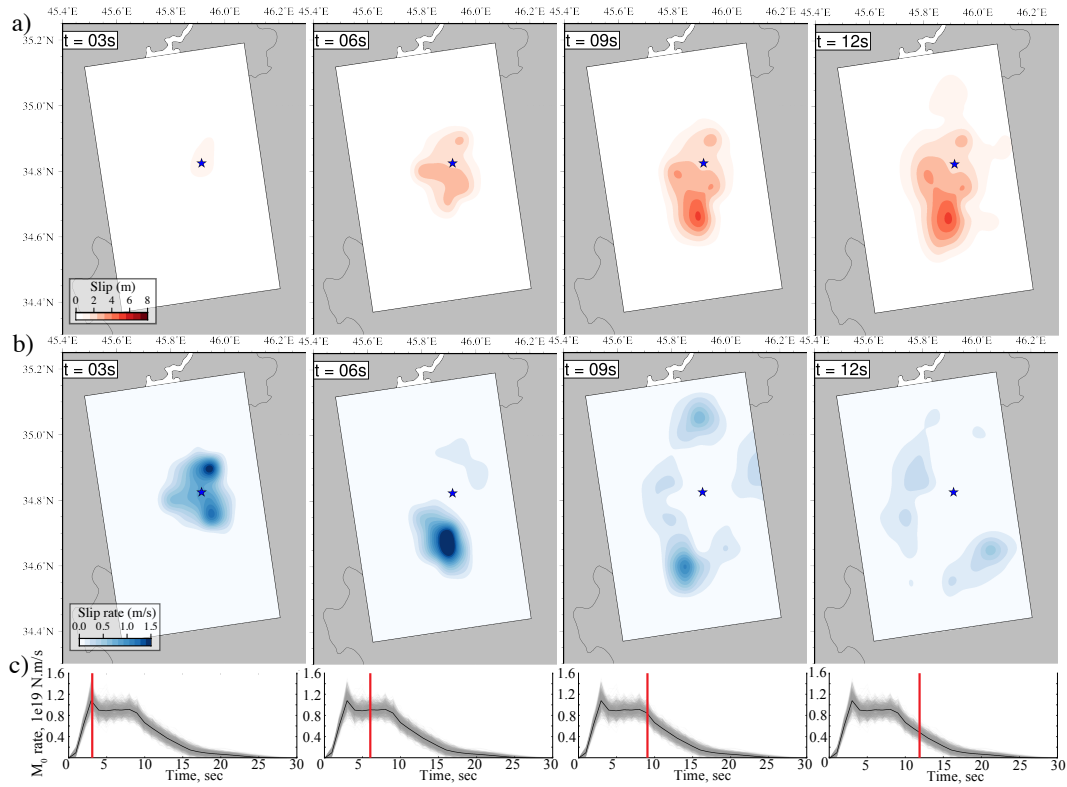
- 492 the Main Recent Fault between 33 and 35 N. *Phil. Trans. R. Soc. Lond. A,*
493 *277(1262)*, 1–25.
- 494 Vajedian, S., Motagh, M., Mousavi, Z., Motaghi, K., Fielding, E., Akbari, B., ...
495 Darabi, A. (2018). Coseismic Deformation Field of the Mw 7.3 12 November 2017
496 Sarpol-e Zahab (Iran) Earthquake: A Decoupling Horizon in the Northern Zagros
497 Mountains Inferred from InSAR Observations. *Remote Sensing*, *10(10)*, 1589.
- 498 Vergés, J., Saura, E., Casciello, E., Fernandez, M., Villaseñor, A., Jiménez-Munt,
499 I., & García-Castellanos, D. (2011). Crustal-scale cross-sections across the NW
500 Zagros belt: implications for the Arabian margin reconstruction. *Geological Maga-*
501 *zine*, *148(5-6)*, 739–761.
- 502 Vernant, P., Nilforoushan, F., Hatzfeld, D., Abbassi, M., Vigny, C., Masson, F., ...
503 others (2004). Present-day crustal deformation and plate kinematics in the Middle
504 East constrained by GPS measurements in Iran and northern Oman. *Geophysical*
505 *Journal International*, *157(1)*, 381–398.
- 506 Walker, R. T., Andalibi, M., Gheitanchi, M., Jackson, J., Karegar, S., & Priestley,
507 K. (2005). Seismological and field observations from the 1990 November 6 Furg
508 (Hormozgan) earthquake: a rare case of surface rupture in the Zagros mountains
509 of Iran. *Geophysical Journal International*, *163(2)*, 567–579.
- 510 Wang, Y., Day, S. M., & Denolle, M. A. (2019). Geometric Controls on Pulse-
511 like Rupture in a Dynamic Model of the 2015 Gorkha Earthquake. *Journal of*
512 *Geophysical Research: Solid Earth*.
- 513 Wanpeng, F., Sergey, S., Rafael, A., Ali, Y., Junhua, L., Qiang, Q., ... Wenjun,
514 Z. (2018). Geodetic constraints of the 2017 Mw7.3 Sarpol Zahab, Iran earth-
515 quake and its implications on the structure and mechanics of the north-west
516 Zagros thrust-fold belt. *Geophysical Research Letters*, *0(ja)*. Retrieved from
517 <https://agupubs.onlinelibrary.wiley.com/doi/abs/10.1029/2018GL078577>
518 doi: 10.1029/2018GL078577
- 519 Yang, Y.-H., Hu, J.-C., Yassaghi, A., Tsai, M.-C., Zare, M., Chen, Q., ... Kam-
520 ranzad, F. (2018). Midcrustal Thrusting and Vertical Deformation Partitioning
521 Constraint by 2017 M w 7.3 Sarpol Zahab Earthquake in Zagros Mountain Belt,
522 Iran. *Seismological Research Letters*, *89(6)*, 2204–2213.



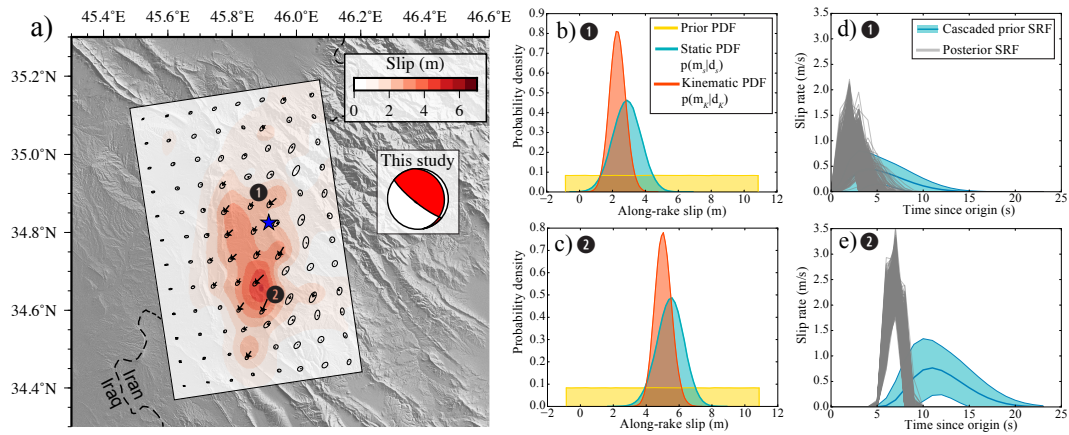
523 **Figure 1. Regional seismotectonic context and damage associated with the 2017 Ezgeleh earth-**
 524 **quake. a)** Blue star marks the epicentre location, and the squares represent the fault parametrisation. Blue
 525 beachball is the moment tensor estimated in this study and brown moment tensors are regional seismicity from
 526 the Global CMT catalogue (Ekström et al., 2012). Red star shows the approximate location of two historical
 527 earthquakes. Dashed black line is the Main Recent Fault (MRF) and dotted lines are supposed location of
 528 regional blind faults (MFF: Mountain Flexure Fault; HZF: High Zagros Fault; ZFF: Zagros Foredeep Fault;
 529 Berberian, 1995). Arrows indicate the convergence of the Arabian plate (AR) with respect to stable Eurasia
 530 (EU) from the GSRM v2.1 (Kreemer et al., 2014) and MORVEL (DeMets et al., 2010) models, computed with
 531 the UNAVCO Plate Motion Calculator. LA: Lorestan Arc. KE: Kirkuk Embayment. Red dashed rectangle
 532 indicates position of b). **b)** Black dots are aftershocks located by the International Institute of Earthquake
 533 Engineering and Seismology of Iran (IIEES). Focal mechanisms from the Global CMT catalogue of three large
 534 aftershocks are shown in green. Brown colours indicate the level of damage based on a compilation of destruc-
 535 tion rate and landslide activity interpolated from field surveys conducted by the Geological Survey of Iran (GSI,
 536 2017). The darker the colour, the more intense the damage. Blue lines are the 1.5 m co-seismic slip contour.



537 **Figure 2. Observations used in the inversion.** a) Unwrapped Sentinel-1A interfer-
 538 ograms showing surface displacement in LOS direction (Track 174). The footprint of one
 539 additional ascending and descending tracks are also shown. Data, predictions and model per-
 540 formance of the 3 interferograms are available in Figures S1-2. b) Location of strong-motion
 541 records (white triangles). c-f) Waveforms of four selected station around the epicenter. For each
 542 waveform, the bold number indicates its maximum amplitude. Φ and d are station azimuth
 543 and distance to epicentre, respectively. The black line is the recorded waveform, grey lines are
 544 stochastic predictions for our posterior model, and the red line is the mean of stochastic predic-
 545 tions. Remaining waveforms are shown in Figure S3.



546 **Figure 3. Temporal evolution of co-seismic slip.** a) Cumulative slip on the fault 3 s, 6 s,
 547 9 s, and 12 s after the origin time. The red colour-scale indicates slip amplitude. b) Evolution of
 548 slip rate on the fault. c) Source time function (STF) of the event. Grey lines are stochastic STFs
 549 inferred from our model population while the black curve represents the posterior mean STF.
 550 Vertical red lines indicate the time of each snapshot.



551 **Figure 4. Final co-seismic slip distribution** a) Colour and arrows on the fault plane
 552 indicate amplitude and direction of slip, respectively. Ellipses represent the 95% posterior un-
 553 certainty. Results presented in subfigures b-e) are obtained for patches labelled 1 and 2. The
 554 background topography comes from the Shuttle Radar Topography Mission (SRTM; Farr et
 555 al., 2007). **b-c)** Prior, posterior static PDF, and posterior kinematic PDF of along-rake slip in
 556 patches 1 and 2. **d-e)** Slip rate evolution in patches 1 and 2. Blue line is the mean prior Slip
 557 Rate Function (SRF) used in the sampling, surrounded by 1- σ uncertainties. Posterior SRFs in
 558 grey are from 1000 thousands models randomly selected from our solution.